Explanation for variability in lower frequency structure-borne noise and vibration: Roles of rear subframe dynamics and right-left spindle phasing

Author, co-author (Do NOT enter this information. It will be pulled from participant tab in MyTechZone)

Affiliation (Do NOT enter this information. It will be pulled from participant tab in MyTechZone)

Abstract

This investigation focuses on a class of rear suspension systems that contain both direct and intersecting structural paths from the tire contact patches to the vehicle body. The structural paths intersect through a dynamically active rear subframe structure. New experiments and computational models are developed and analyzed in this article to investigate the variability of structure-borne noise and vibration due to tire/road interactions in the lower- to mid-frequency regimes. Controlled operational experiments are conducted with a mass-production minivan on a chassis dynamometer equipped with rough road shells. Unlike prior literature, the controlled experiments are analyzed for run-run variations in the structure-borne noise up to 300 Hz in a single vehicle to evaluate the nature of excitations at the spindle as the key source of variation in the absence of significant manufacturing, assembly and instrumentation errors. Further, a deterministic modal expansion approach is used to examine these variations. Accordingly, an illustrative eleven-degree-of-freedom lumped parameter half vehicle model is developed and analytically utilized to demonstrate that left-right spindle excitation phasing dictates the participation of the subsystem vibrational modes in the system forced response. The findings are confirmed through the analysis of a reduced finite element model of the vehicle system with a high-fidelity, modally dense suspension model, where the left-right rolling excitation phasing at the spindle alone is found to affect the component dynamic vibration amplitudes up to ±30 dB depending upon the component location and frequency range. These results are in qualitative agreement with the type of variations observed in the experiments.

Keywords: operational experimental studies, vehicle models, vibration modes, vehicle subframes, structural transfer paths

Introduction

Variability in vehicle vibration, structure-borne noise and interior noise levels due to tire-road interactions has been studied for at least two decades [1,2], as evident from the literature survey by Lalor and Prieibsch [1]. Several statistical studies have found variability in measured noise and vibration data for nominally identical vehicles [3-8]. In particular, Kompella and Bernhard [3] used a large sample of 99 nominally identical vehicles to study variations in both structure-borne and air-borne frequency response functions; they reported that the most significant variations were due to manufacturing and assembly differences when measurement variations are controlled. While a significant body of literature exists on variations in structural frequency responses and modal parameters [4], fewer attempts have been made to examine vibro-acoustic variations under operational loads [5,6,8]. To fill this void, this article proposes a deterministic modal expansion approach to examine variations in structure-borne noise at the lower frequency end (from 30 to 300 Hz). Further, this article explores the contribution of the left-right rolling excitation phasing at the spindle to run-run variations in acoustic-structural parameters that occur during operational dynamometer experiments and to develop minimal order dynamic and finite element models to provide plausible explanations for the underlying physics.

Problem formulation

The focus of this article is on a class of rear suspension systems where a metallic subframe creates an intersecting structural path between the left and right tire contact patches and the vehicle body. A schematic of such a system is provided in Fig. 1 with ten multi-dimensional structural paths between the tire contact patch and the vehicle body in the form of four connections via the subframe and two connections each via the left and right trailing arms, dampers and suspension springs. A simplified dynamic model, which reduces the number of paths to four single-dimension paths while retaining the intersecting structural paths via a subframe representation, will be proposed in this article. The chief objectives of this article are as follows: 1. Examine run-run variations in measured structural-acoustic responses under controlled operational rolling-tire experiments on one vehicle; 2. Develop and analyze two formulations (a high-fidelity finite element and then minimal order lumped parameter model) to examine the role of the left-right excitation phasing at the spindles on the subframe responses; 3. Provide explanations for variability while examining the physics of this problem; and 4. Compare the finite element model with operational measurements.

The subject of this article is limited to linear time-invariant system and frequency domain methods with assumed loss factors. The frequency range is limited from 30 Hz to 300 Hz, as this is the range within which structure-borne road noise and vibration phenomena of interest (from the perspective of subframes) occur. Accordingly, both finite element and lumped models include only structural representations of components from the spindle to the vehicle body and explicitly ignore the tires, wheels, and cabin acoustics since there is significant complexity involved in the development of accurate models of the entire vehicle system. For instance, current tire models described in the literature [9] may not be valid over broad-range frequencies, and there is a lack of well-established experimental data to validate computational models. In this work, the suspension is excited by imposing (assumed) motions at the left and right spindles. While the inclusion of the vehicle body may provide stronger correlations in the lower-frequency ranges, accurate modeling of dynamic interactions between the vehicle body, suspension system and tires is beyond the

scope of this article. Only the deterministic nature of the variations in the operational tests is examined using both sound and vibration spectra as well as operational deflection shapes, which serve as good visualization tools to study the subframe dynamics under real operating conditions.

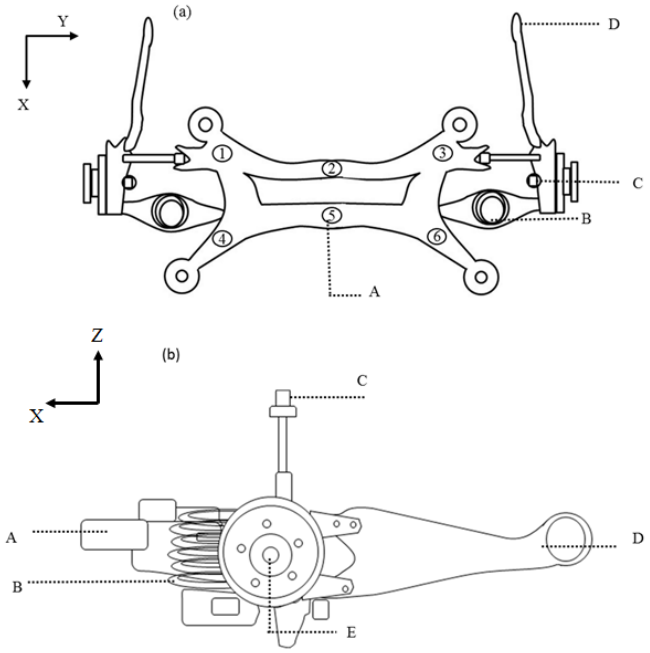

Figure 1: Schematic of rear suspension (a) top view; (b) side view; key- A, subframe; B, suspension spring; C, damper; D, trailing arm; E, spindle center; locations for accelerometers on the subframe are given by 1–6.

Operational vehicle measurements

Controlled vehicle measurements on a chassis dynamometer are conducted on a front wheel drive, mass-production minivan. Only the rear wheels of the vehicle are driven over the rough-road textured rollers, and both the left and right textures are constructed from identical molds and oriented 180 degrees from left-to-right. Microphones (TMS T130C21, typical sensitivity - 20 mV/Pa) are placed at the driver's left and right ear positions to measure the cabin sound pressures, and tri-axial accelerometers (Dytran instruments, 32723-A-2, typical sensitivity - 100 mV/g) are placed on many locations of the rear suspension, including six on the rear subframe as shown in Fig. 1. The placement of 6 accelerometers permits the capture of the rigid body modes and first three flexural modes of this particular subframe. Only the steady-state measurements of sound pressure levels (L_p, dB re 20 μPa) at the driver's ears and accelerations (dB re 1.0 g rms) at the suspension locations are made at roller speeds of 40, 80, and 120 kph. Since variations are observed of the same magnitudes for each roller speed, only the 80 kph results are shown. Further, constant roller speeds are intentionally selected to remove the complexity of speed-dependent rolling-tire properties from the analysis. Each narrow-band spectrum is based on 50 averages of signals acquired at a sampling rate of 1024 Hz with a resolution of 2 Hz up to 512 Hz.

Three identical runs of this experiment are performed, and the measured sound pressure and acceleration levels are compared for variations on a narrow-band basis. Fig. 2(a) shows variations in L_p measured at the driver's left ear, and Fig. 2(b) displays a hatch plot where the area depicts the variations in L_p observed over the three runs. The upper and lower limits of this hatch are formed by computing the maximum and minimum L_p levels measured. The difference between these two sound pressure levels, ΔL_p, is shown in Fig. 2(c). While a maximum variation of about 25 dB(A) is found, somewhat minimal variations at some of the major peaks in the spectra are observed. The vertical acceleration levels for location 1 on the rear subframe and for the spindle center are illustrated in Figs. 3 and 4, respectively. The hatch plots in Figs. 3(b) and 4(b) follow a trend similar to the sound pressure spectra, and this confirms that the structure-borne noise is the dominant path. Further, maximum

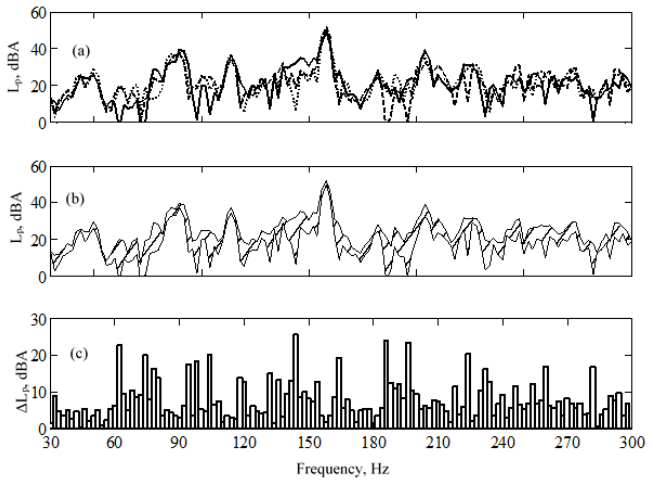

Figure 2: Measured sound pressure level spectra (L_p, dBA re 20 μPa) at the driver's left ear (DLE) on a 2 Hz narrow-band basis from 30-300 Hz (a) run-run variations: — , Run 1; ----, Run 2; -----, Run 3; (b) hatch plot representation of the run-run variations; (c) difference between maximum and minimum sound pressure levels (ΔL_p, dBA) at each frequency.

variations of 23 dB and 28 dB are observed in the measured accelerations at the subframe and spindle, respectively (Figs. 3(c) and 4(c)); but some of the major peaks remain less sensitive to variations, as observed in the sound pressure levels. Since the experiment is conducted on the same vehicle without any changes to the instrumentation system and setup, the main source of the observed changes could be attributed to variation in the orientation of the tires on the textured rollers between the three runs. The consistency in the peak responses observed in the sound or acceleration spectra for the identical three runs further confirms that assembly and measurement are not the sources of variations.

Next, measured operational deflection shapes (ODS) are utilized to visualize and understand the physical meaning of these variations. The displacement responses, at a selected excitation frequency, acquired at six locations on the subframe (shown as 1 to 6 in Fig. 1) are used to construct these ODS displays. The forced response is captured in each view as a trajectory scaled by a factor for visualization purposes; these trajectories are then superimposed on the subframe schematics to enhance visualization. The locations at which trajectories are made are marked in Fig. 5 by shaded circles, while the open squares indicate the starting point. Based on averaged variations between the runs at the six different locations on the subframe, ODS at 244 Hz with a high variation is selected to illustrate the subframe dynamics. Four views (top, front, left and right) are displayed in Fig. 5 for the deflection shapes, and a comparison is made between the three runs. In run 1, the trajectory of location 2 (subframe cross member) is a motion that can

be visualized as a combination of motion seen in the schematic for the XY and XZ view. However, in run 2 the rotation in the XZ plane is in a different direction and orientation, and the angular motion found in runs 1 and 2 is non-existent in run 3. The ODS display further establishes the participation of the subframe in the 150-250 Hz frequency range of interest and their possible sensitivity to excitation variations between the runs.

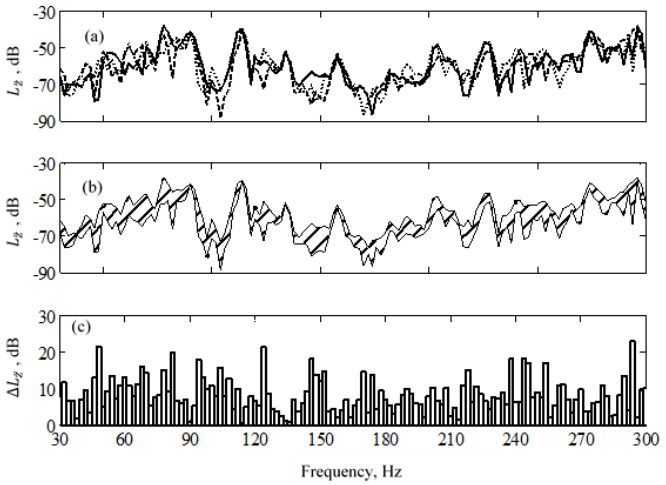

Figure 3: Measured acceleration spectra ($L_{\ddot{z}}$, dB re 1.0 g rms) on the rear subframe (at location 1 as shown in Fig. 1), on a 2 Hz narrow-band basis from 30-300 Hz (a) run-run variations: ——, Run 1; ----, Run 2; ·····, Run 3; (b) hatch plot representation of the run-run variations; (c) difference between maximum and minimum acceleration response ($\Delta L_{\ddot{z}}$, dB) at each frequency.

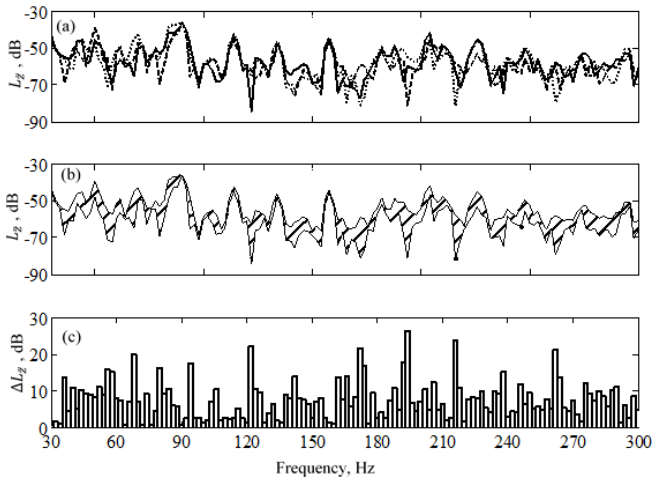

Figure 4: Measured acceleration spectra ($L_{\ddot{z}}$, dB re 1.0 g rms) at the spindle center at 2 Hz resolution (E in Fig.1). (a) run-run variations: ——, Run 1; ----, Run 2; ·····, Run 3; (b) hatch plot representation of the run-run variations; (c) difference between maximum and minimum acceleration response ($\Delta L_{\ddot{z}}$, dB) at each frequency.

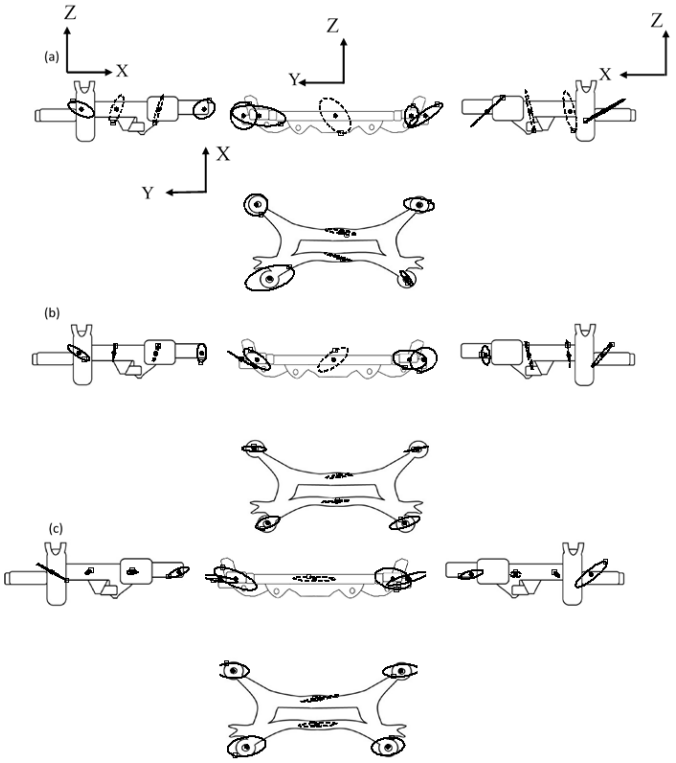

Figure 5: Measured operational deflection shape of subframe at 244 Hz (a) Run 1 (b) Run 2 (c) Run 3:● ,locations on the subframe where deflections are measured; □, trajectory starting point (at t = 0); — , trajectory.

Development of high-fidelity finite element model

A high-fidelity computational model of a rear-half vehicle is developed to study the physics behind the run-run variations observed in operational experiments. The vehicle body is assumed to be rigid (ground) and massive relative to the rear suspension components in the finite element model shown in Fig. 6. The subframe and other suspension components are connected to the rigid

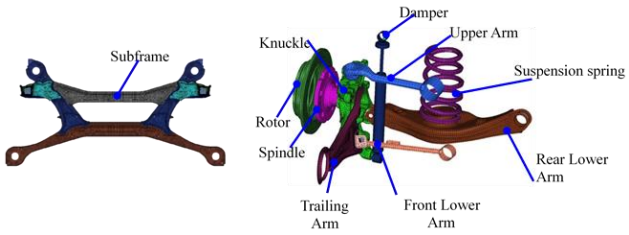

Figure 6: Finite element model of the rear suspension.

vehicle body via bushings represented by stiffness and damping elements. In addition, the tires, wheels, and cabin acoustics are explicitly ignored to simplify modeling complexities. Here the subframe consists of 63,000 shell elements (in ABAQUS [10]), and the other suspension system is described by 155,350 shell and solid elements. A component-by-component modal analysis of the rear suspension model under free-free boundary conditions reveals that certain components, such as the dampers, suspension springs, subframe and trailing arms, have a relatively more significant modal participation with up to 10 modes in the frequency range of interest (30-300 Hz). The eigenvalue analysis of the full rear suspension model reveals that this system is modally dense, with as many as 96 modes in

the 30-300 Hz range of which 65 modes lie in the 150-300 Hz range, where the subframe is found to have significant modes. Based on this observation, the finite element model is further reduced to ignore few non-participating components, such as the brake pads and rotors, with the reduced model consisting of a total of 163,000 elements. Structural damping is the primary damping mechanism considered for the suspension model, with the metallic components assigned a nominal loss factor of 0.001. The axial properties of the hydraulic damper are assumed to be viscously damped, and the component connector elements (such as bushings) are assumed to be damped and thus given by a complex-valued stiffness element, where γ is the assumed loss factor (1 to 20% depending on the component):

$$\tilde{k} = k(1 + i\gamma). \tag{1}$$

Development of an illustrative, reduced order model of rear-half vehicle

Since no significant literature exists on lumped parameter models for studies of this nature, an iterative process is adopted to develop a lumped model to study the underlying system physics and qualitatively correlate with the finite element model. As the excitation from the tire is primarily in the vertical direction [11] for road noise and vibration problems, a lumped model with only vertical degrees of freedom is developed. Since the rear suspension system of interest has intersecting transfer paths through a dynamically active subframe, a minimal order lumped parameter model of 11 degrees of freedom, which captures two of the transfer paths (suspension springs) from the spindle to the vehicle body in addition to the subframe, is developed as illustrated in Fig. 7.

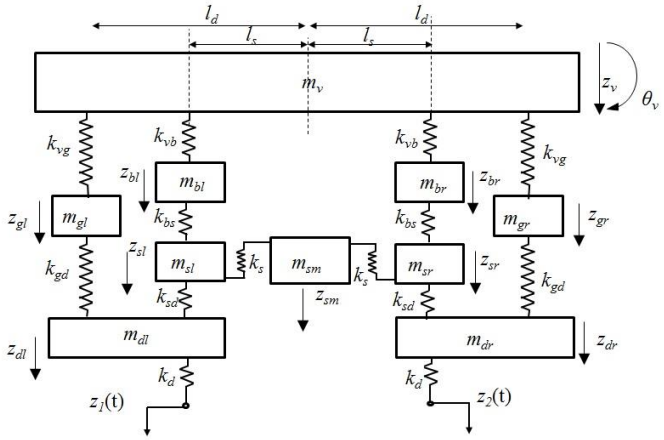

Figure 7: Lumped model (11 DOF) of the vehicle system (half-car type approximation). Refer to the list of symbols in the text for identification of symbols, including subscripts.

The vehicle body is considered as a single (massive/rigid) lumped mass (m_v) with one translational coordinate (z_v) and one rotational coordinate (θ_v), where the subscript v denotes vehicle body. m_v is assumed to be about 30% of the vehicle mass. The moment of inertia of vehicle body (I_v) is calculated as $I_v = m_{vl}\, m_{vr}\, l^2/(m_{vl} + m_{vr})$, where m_v is approximated by two lumped masses (m_{vl} and m_{vr}) on the left (subscript l) and right (subscript r) extremities of a massless rod of length l. Assuming $m_{vl} = m_{vr} = m_v/2$, the above expression reduces to $I_v = m_v\, l^2/4$. The vehicle subframe is approximated by a simple three-degree-of-freedom semi-definite system with only vertical displacements z_{sl}, z_{sm} and z_{sr}, where subscript s denotes the subframe and subscripts l, m and r denote left, middle and right, respectively. This model consists of masses m_{sl}, m_{sm} and m_{sr} connected by a bushing connector element with an elastic stiffness k_s. The parameter values are chosen such that the first two flexural modes of the subframe are captured in terms of both the natural frequencies and dominant vertical mode shape. The static stiffness of the subframe must be evaluated from the finite element model in order to assess relevant mass and stiffness parameters for the subframe lumped model. Four different iterations are considered, and the corresponding computed static stiffness and the lumped mass values to physical subframe mass (as a ratio) are analyzed. The iterations involve different boundary conditions and loading schemes at the connection points between the subframe, the vehicle body and the other suspension components. The subframe is attached to the vehicle body through bushings via four connection points, one at each corner of the subframe arms, and it is connected to the other suspension components via four connection points located at the bottom of the subframe, with two connections each to the left and right half of the suspension components. For case 1, the four connections on the subframe arms and two of the connections (one on each side) at the bottom of the subframe, which are located farther away from the middle of the subframe, are clamped. The other two connections at the bottom, which are closer to the middle of the subframe, have their rotational degrees of freedom arrested, and two equal amplitude static loads, 0.5P, are applied. The static stiffness is calculated by dividing the average of the static load by the average of the static deflections δ computed at the driving points. This yields a high stiffness and a lumped mass that is 2.5 times the actual subframe mass. In case 2, the clamped connections from case 1 are replaced by pinned connections, and similar static loads are applied. The pinned connections lower the static stiffness, but this value still yields a high mass ratio, which is not desirable. In case 3, the pinned connections at the lower section of the subframe are changed to free boundary conditions, and using the computed stiffness, a mass ratio of 1 is achieved. In case 4, the connections on one side are clamped, and the vertical static load is applied on the other side, but this results in an order of magnitude reduction in the mass ratio, which again is undesirable. Hence, case 3 is chosen to be the best case to capture both the natural frequencies and the flexural modes of the subframe.

The left and right subframe masses are connected to the vehicle body through bushings represented by masses m_{bl} and m_{br}, where the subscript b denotes bushing. The stiffness elements k_{vb} (= k_{bs}), where subscripts vb and bs denote the connections between vehicle and bushing, and subframe and bushing, respectively, are calculated as $k_{vb}k_{bs}/(k_{vb}+k_{bs}) = k_{vb}/2 = k_{bz1}$, where k_{bz1} property is obtained from the finite element model. Similarly, the spindle masses, m_{dl} and m_{dr}, where subscript d denotes spindle, are connected to the subframe masses through bushing stiffness elements k_{sd} (= k_d) computed as k_{sd} $k_d/(k_{sd}+k_d) = k_{sd}/2 = k_{bz2}$, where the parameter k_{bz2} is obtained from the finite element model. Knowing k_{vb} and k_{bs}, and considering a single-degree-of-freedom approximation for the bushing where the spring elements are both connected to the ground, the masses m_{bl} and m_{br} can be calculated using $f_n = 1/2\pi\sqrt{(k_{vb}+k_{bs})/m_{bl}}$, such that the natural frequency f_n is equal to 500 Hz.

The path through the suspension springs is approximated using masses m_{gl} and m_{gr}, where subscript g denotes the suspension spring and stiffness k_{gd} and k_{vg}. Similar to the subframe static stiffness calculations, the static stiffness of the finite element model of the spring is computed. Using a single-degree-of-freedom approximation similar to the bushing approximation, the static stiffness value and the effective mass of the spring are computed.

Real eigensolution of the lumped vehicle model

The equations of motion of the lumped system of Fig. 7 are as follows:

$$m_v\ddot{z}_v + 2(k_{vg} + k_{vb})z_v - k_{vb}z_{bl} - k_{vb}z_{br} - k_{vg}z_{gl} - k_{vg}z_{gr} = 0 \quad (2a)$$

$$J_v\ddot{\theta}_v + 2\left(k_{vg}l_2^2 + k_{vb}l_1^2\right)\theta_v + k_{vb}l_1z_{bl} - k_{vb}l_1z_{br} + k_{vg}l_2z_{gl} \ldots - k_{vg}l_2z_{gr} = 0 \quad (2b)$$

$$m_{bl}\ddot{z}_{bl} + (k_{vb} + k_{bs})z_{bl} - k_{vb}z_v + k_{vb}l_1\theta_v - k_{bs}z_{sl} = 0 \quad (2c)$$

$$m_{br}\ddot{z}_{br} + (k_{vb} + k_{bs})z_{br} - k_{vb}z_v - k_{vb}l_1\theta_v - k_{bs}z_{sr} = 0 \quad (2d)$$

$$m_{gl}\ddot{z}_{gl} + \left(k_{vg} + k_{gd}\right)z_{gl} - k_{vg}z_v + k_{vg}l_2\theta_v - k_{gd}z_{dl} = 0 \quad (2e)$$

$$m_{gr}\ddot{z}_{gr} + \left(k_{vg} + k_{gd}\right)z_{gr} - k_{vg}z_v - k_{vg}l_2\theta_v - k_{gd}z_{dr} = 0 \quad (2f)$$

$$m_{sl}\ddot{z}_{sl} + (k_{bs} + k_s + k_{sd})z_{sl} - k_{bs}z_{bl} - k_sz_{sm} - k_{sd}z_{dl} = 0 \quad (2g)$$

$$m_{sm}\ddot{z}_{sm} + 2(k_s)z_{sm} - k_sz_{sl} - k_sz_{sr} = 0 \quad (2h)$$

$$m_{sr}\ddot{z}_{sr} + (k_{bs} + k_s + k_{sd})z_{sr} - k_{bs}z_{br} - k_sz_{sm} - k_{sd}z_{dr} = 0 \quad (2i)$$

$$m_{dl}\ddot{z}_{dl} + \left(k_{sd} + k_d + k_{gd}\right)z_{dl} - k_{sd}z_{sl} - k_{gd}z_{gl} = k_dz_1 \quad (2j)$$

$$m_{dr}\ddot{z}_{dr} + \left(k_{\mathrm{sd}} + k_d + k_{gd}\right)z_{dr} - k_{sd}z_{sr} - k_{gd}z_{gr} = k_dz_2, \quad (2k)$$

where $\ddot{z}$ and z are the dynamic acceleration and displacements of the masses, and $\ddot{\theta}$ and θ are the dynamic rotational acceleration and displacements, with the other subscripts having the same meaning as defined before. Subscripts 1 and 2 in Eqns. (2j) and (2k) denote the excitation index corresponding to the dynamic motions applied at the spindle masses. The corresponding system parameters are summarized in Table 1. All spring elements in the lumped system are assumed to be damped modeled by a complex valued stiffness, as given by Eq. (1), where γ is the assumed loss factor. For instance, γ is assumed to be 1% and 3% for the subframe and suspension springs, respectively, as these are typically lightly damped. The γ values for the bushing stiffness and spindle stiffness are assumed to be 10% similar to the finite element model. Ignoring structural damping in the system, the system equations can be written in the form as follows, where $\underline{\underline{M}}$ is the mass matrix, $\underline{\underline{K}}$ is the stiffness matrix, $\underline{z}$ is the displacement vector, and $\underline{F}$ is the excitation force/moment vector:

$$\underline{\underline{M}}\,\underline{\ddot{z}} + \underline{\underline{K}}\,\underline{z} = \underline{F}. \quad (3)$$

The real eigensolution of Eq. (3) is computed using the values in Table 1, and the predicted natural frequencies of the system are 11.1, 21.2, 74.0, 74.0, 131.3, 162.2, 203.5, 377.4, 383.1, 516.9 and 517.6 Hz. It is observed that the low frequencies (below 30 Hz) are dominated by the vehicle body modes (modes 1 and 2), and the higher frequencies (beyond 350 Hz) are dominated by the bushing masses as expected. In particular, modes 5 (131.3 Hz), 6 (162.2 Hz) and 7 (203.5 Hz) are dominated by the three subframe mass element motion. Specifically, modes 5 and 7 are affected by the subframe mass m_{sm}, (representative of the subframe cross members), and mode 6 is influenced by the other two subframe masses m_{sl} and m_{sr}.

Table 1: Parameters for the lumped vehicle model of Fig. 7.

Parameter (units)	Value	Parameter (units)	Value
m_v (kg)	240	k_{vb}, k_{bs} (N/mm)	$5\text{x}10^4$
m_{bl} (kg)	0.98	k_{sd}, k_d (N/mm)	$3\text{x}10^4$
m_{br} (kg)	0.98	k_s, k_{vg}, k_{gd} (N/mm)	$5\text{x}10^2$
m_{gl} (kg)	0.75	γ_{vb}, γ_{bs}, γ_{sd}, γ_d	0.1
m_{gr} (kg)	0.75	γ_s	0.01
m_{sl} (kg)	8	γ_{gd}, γ_{vg}	0.03
m_{sm} (kg)	8		
m_{sr} (kg)	8		
m_{dl} (kg)	30		
m_{dr} (kg)	30		
I_v (kg-m^2)	194		

In addition to capturing the first two natural frequencies of the subframe in the free-free boundary conditions, the lumped model also successfully captures the natural frequencies of the subframe under realistic boundary conditions. However, the modes from the subframe lumped model only approximate the vertical deflections of the flexural modes. Since this 11-degree-of-freedom model captures the modal properties reasonably well, it will be used to study the subframe dynamics under dynamic excitation conditions.

Forced response analysis using real eigensolutions

The steady-state harmonic response of the lumped model is computed by applying sinusoidal displacement excitations z_1 and z_2 (of unit amplitude but varying phase), where subscripts 1 and 2 denote the excitation index at the spindle masses m_{dl} and m_{dr}, respectively. The system responses are computed for two limiting cases of displacement excitations at the left and right spindles: (i) equal in-phase excitations ($z_1 = z_2$) and (ii) equal out-of-phase excitations ($z_1 = - z_2$). Due to left-right symmetry in the system, the steady-state accelerations of the left and right masses of the suspension springs, bushings, subframe and spindle are identical. The subframe accelerations for two input excitation phasing cases are illustrated in Figs. 8 and 9. Resonance peaks are observed at 130 and 204 Hz and an anti-resonance around 190 Hz for the in-phase excitation. In contrast, for the out-of-phase excitation, a resonance peak occurs around 163 Hz, corresponding to mode 6, while modes at 130 Hz and 204 Hz are not excited. These preliminary results suggest that large variations in response can occur due to phasing between excitations at the spindles. This is analyzed further using the modal expansion theorem [12]. The solution to Eq. (3) is written as a linear combination of vibration modes of the system as:

$$z(t) = \eta_1(t)\underline{\phi}^{(1)} + \eta_2(t)\underline{\phi}^{(2)} + \cdots + \eta_{11}(t)\underline{\phi}^{(11)}, \tag{4}$$

where $\eta_i(t)$ are the modal participation coefficients for i = 1, 2, 3,…..11 and $\underline{\phi}^{(i)}$ denotes the i[th] modal vector, which is assembled into a modal matrix as:

$$\underline{\underline{\phi}} = [\underline{\phi}^{(1)}\ \underline{\phi}^{(2)}\ \underline{\phi}^{(3)}\ \underline{\phi}^{(4)}\ \ldots.\underline{\phi}^{(11)}]. \tag{5}$$

Rewrite Eqs. (4) and (5) as follows, where $\underline{\eta}(t) = [\eta_1(t)\ \eta_2(t)\ \ldots\ldots\eta_{11}(t)]^T$ and the superscript T denotes transpose,

$$\underline{z}(t) = \underline{\underline{\phi}}\,\underline{\eta}(t). \tag{6}$$

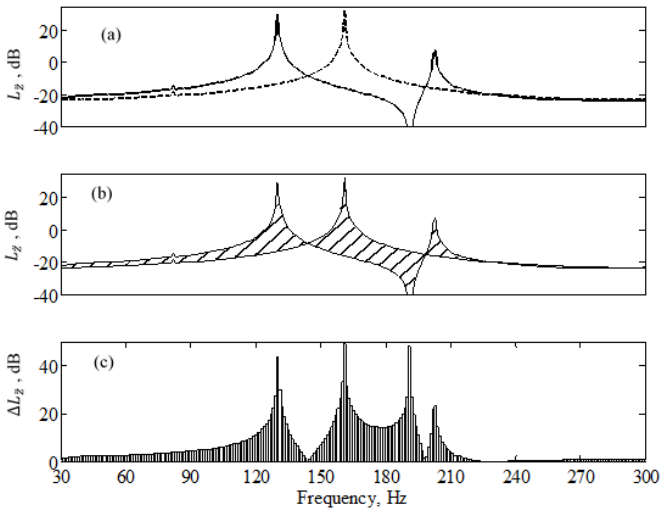

Figure 8: Computed acceleration spectra at the subframe left mass m_{sl}, ($L_{\ddot{z}}$, dB re 1.0g rms) using the lumped vehicle model of Fig. 2 shown at 1-Hz resolution: (a) results for in-phase (——, 0°) and out-of-phase (---, 180°); (b) hatch plot representation of phasing variations; (c) difference between maximum and minimum acceleration response at each frequency ($\Delta L_{\ddot{z}}$, dB).

Further define the acceleration vector as: $\underline{\ddot{z}}(t) = \underline{\underline{\phi}}\,\underline{\ddot{\eta}}(t)$. The force vector in the modal domain, $\underline{Q}$ is defined as:

$$\underline{Q} = \underline{\underline{\phi}}^T\underline{F}(t), \tag{7}$$

where $\underline{F}(t) = [0\ 0\ 0\ 0\ 0\ 0\ 0\ 0\ 0\ 0\ F_1\ F_2]^T$, with F_1 and F_2 denoting dynamic force excitations at the left and right spindles. Using Eqs. (6) and (7), Eq. (3) can be rewritten in terms of uncoupled, undamped differential equations of second order:

$$\underline{\ddot{\eta}}(t) + [\ddots\ \Omega_i^2\ \ddots]\underline{\eta}(t) = \underline{Q}(t), \tag{8}$$

where Ω_i denotes the i[th] natural frequency of the system. The steady-state harmonic response for undamped oscillators in the modal domain is given by:

$$\eta_i = \frac{Q_i}{\Omega_i^2 - \omega^2}\ . \tag{9}$$

The steady-state response in the physical domain is then computed using Eq. (6), which is expanded as follows:

$$\begin{aligned} z_v &= \phi_v^{(1)}\eta_v + \phi_v^{(2)}\eta_\theta + \cdots\ \phi_v^{(11)}\eta_{dr} \\ &\ \ \vdots \quad\ \ \vdots \quad\ \ \vdots \quad\ \ \vdots \\ z_{dr} &= \phi_{dr}^{(1)}\eta_v + \phi_{dr}^{(2)}\eta_\theta + \cdots\ \phi_{dr}^{(11)}\eta_{dr}. \end{aligned} \tag{10}$$

The acceleration response is subsequently calculated by the relation $\ddot{z}_i = -\omega^2 z_i$. From Eq. (10), the harmonic response is dependent on both the modal matrix $\underline{\underline{\phi}}$ and the modal responses $\underline{\eta}$. To study this further, each term of Eq. (10) is plotted individually and compared with the total physical response; minimal damping is assumed in each case to ensure bounded responses at the resonances. Fig. 10(a, b) compares the computed accelerations (with a frequency resolution of 1 Hz) at the left subframe mass m_{sl} for the in-phase and the out-of-phase excitations. Up to 300 Hz, the motion terms associated with m_v (only θ_v), m_{bl}, m_{gl}, m_{sl}, m_{sr} and m_{dl} are dominant for in-phase excitation. In contrast, the motion terms associated with m_v (only z_v), m_{br}, m_{gr}, m_{sm} and m_{dr} are dominant for the out-of-phase case. In order to further examine why certain modes are not excited for a particular excitation, the modal force vector is studied by expanding Eq. (7) as:

$$Q = [\underline{\phi}^{(1)}\ \underline{\phi}^{(2)}\ \underline{\phi}^{(3)}\ \underline{\phi}^{(4)}\ \ldots.\underline{\phi}^{(11)}]^T \begin{bmatrix} 0 \\ 0 \\ 0 \\ 0 \\ 0 \\ 0 \\ 0 \\ 0 \\ 0 \\ F_1 \\ F_2 \end{bmatrix} \tag{11a}$$

$$= \begin{bmatrix} \phi_{dl}^{(1)}F_1 + \phi_{dr}^{(1)}F_2 \\ \phi_{dl}^{(2)}F_1 + \phi_{dr}^{(2)}F_2 \\ \vdots \\ \vdots \\ \vdots \\ \vdots \\ \phi_{dl}^{(11)}F_1 + \phi_{dr}^{(11)}F_2 \end{bmatrix}. \tag{11b}$$

Observe from Eq. (11b) that the terms influencing the modal force vector are the eigenvectors corresponding to the left and right spindle masses m_{dl} and m_{dr}. It is clear that these eigenvectors are in-phase with

each other at modes 2, 3, 5, 7, 9 and 10 and out-of-phase with the other modes as shown in Table 2. This implies that for an in-phase excitation ($F_1 = F_2$), the modes 1, 4, 6, 8 and 11 (out-of-phase modes) would lead to a cancellation of forces; in contrast, for an out-of-phase excitation ($F_1 = -F_2$), the modes 2, 3, 5, 7, 9 and 10 (in-

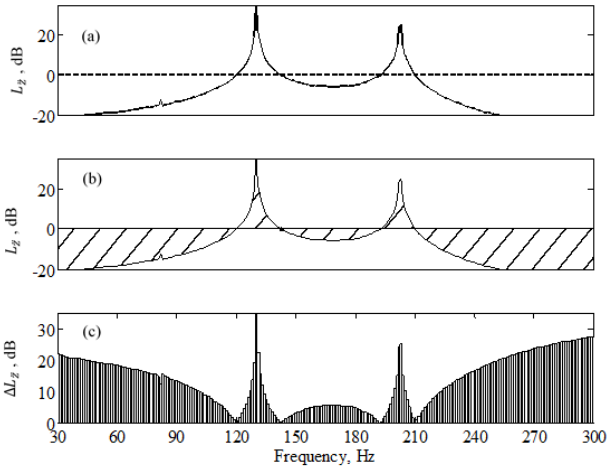

Figure 9: Computed acceleration spectra at the subframe middle mass m_{sm}, ($L_{\ddot{z}}$, dB re 1.0g rms) using the lumped vehicle model of Fig. 2 shown at 1-Hz resolution: (a) results for in-phase (——, 0°) and out-of-phase (---, 180°); (b) hatch plot representation of phasing variations; (c) difference between maximum and minimum acceleration response at each frequency ($\Delta L_{\ddot{z}}$, dB).

phase modes) would lead to a cancellation of forces. The modal forces are as shown in Table 3, and this explains why only 6 modes are present in Fig. 10(a) and the remaining in Fig. 10(b).

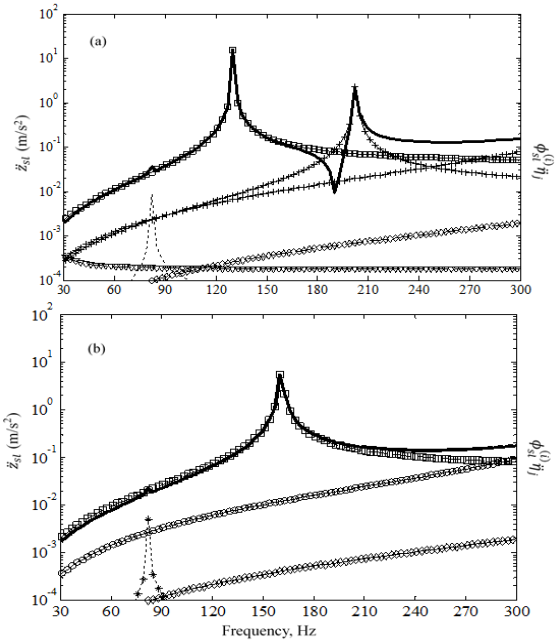

Figure 10: Computed acceleration spectra of modal masses corresponding to the lumped vehicle model with minimal possible damping: (a) In-phase excitation case; (b) Out-of-phase excitation case:—, $\ddot{z}_{sL}$; ——, $\phi_{sL}\ddot{\eta}_{zv}$; – –, $\phi_{sL}\ddot{\eta}_{\theta v}$; …, $\phi_{sL}\ddot{\eta}_{bL}$; * , $\phi_{sL}\ddot{\eta}_{bR}$; –□–, $\phi_{sL}\ddot{\eta}_{gL}$; – –□–, $\phi_{sL}\ddot{\eta}_{gR}$; –|–, $\phi_{sL}\ddot{\eta}_{sL}$; –o–, $\phi_{sL}\ddot{\eta}_{sM}$; – –|–, $\phi_{sL}\ddot{\eta}_{sR}$; –◊–, $\phi_{sL}\ddot{\eta}_{dL}$; – –◊–, $\phi_{sL}\ddot{\eta}_{dR}$.

Table 2: Real and complex eigenvectors for left and right spindles.

	Real eigen-values	Real eigenvectors		Complex eigenvalues $\Omega^2 = \omega_n^2(1+j\eta)$		Complex eigenvectors (given non-proportional damping)	
Mode	$\omega_n/2\pi$ (Hz)	Left ϕ_{dl}	Right ϕ_{dr}	$\omega_n/2\pi$ (Hz)	η	Left $\tilde{\psi}_{dl}$	Right $\tilde{\psi}_{dr}$
1	11.1	0.002	-0.002	11.1	0.093	-0.021 +0.003j	-(-0.021 +0.003j)
2	21.1	0.005	0.005	21.1	0.099	0.003 -0.068j	0.003 -0.068j
3	82.2	0.003	0.003	82.2	0.030	-0.002 +0.001j	-0.002 +0.001j
4	82.2	-0.002	0.002	82.2	0.030	0.001 -0.001j	-(0.001 -0.001j)
5	129.9	0.083	0.083	130.0	0.084	0.342 +0.023j	0.342 +0.023j
6	160.5	0.114	-0.114	160.5	0.087	0.573 +0.412j	-(0.573 +0.412j)
7	200.5	-0.08	-0.08	200.6	0.039	-0.272 +0.010j	-0.272 +0.010j
8	376.0	0.06	-0.06	376.0	0.092	0.254 +0.005j	-(0.254 +0.005j)
9	381.3	0.056	0.056	381.2	0.087	-0.219 -0.025j	-0.219 -0.025j
10	515.6	-0.010	0.010	515.6	0.099	-0.004 +0.011j	-(-0.004 +0.011j)
11	516.2	0.010	0.010	516.2	0.099	-0.015-0.0004j	-0.015 -0.0004j

Forced response analysis using complex eigensolutions

The effect of damping is examined next by evaluating complex eigensolutions. The system equations are of the form similar to Eq. (7), except here $\underline{\underline{K}}$ is a complex-valued stiffness matrix with elements of the form $k(1+i\gamma)$ as is assumed in the finite element model. The complex eigenvalue problem is solved first to obtain the mass normalized complex eigenvectors $\underline{\underline{\tilde{\psi}}}$. Like the previous section, the modal expansion principle is applied to rewrite Eq. (3) as:

$$\underline{\underline{M}}\,\underline{\underline{\tilde{\psi}}}\,\ddot{\underline{\eta}} + \underline{\underline{\tilde{K}}}\,\underline{\underline{\tilde{\psi}}}\,\underline{\eta} = \underline{F}. \tag{12}$$

Pre-multiplying Eq. (12) by the Hermitian transpose (superscript HT) of the complex modal matrix $\underline{\underline{\tilde{\psi}}}$ to yield:

$$\underline{\underline{\tilde{\psi}}}^{HT}\underline{\underline{M}}\,\underline{\underline{\tilde{\psi}}}\,\ddot{\underline{\eta}} + \underline{\underline{\tilde{\psi}}}^{HT}\underline{\underline{K}}\,\underline{\underline{\tilde{\psi}}}\,\underline{\eta} = \underline{\underline{\tilde{\psi}}}^{HT}\underline{F}\,, \tag{13}$$

which upon simplification yields 11 decoupled equations as:

$$\ddot{\underline{\eta}} + [\ddots\ \tilde{\lambda}_i^2\ \ddots]\underline{\eta} = \underline{Q}, \tag{14}$$

where $\tilde{\lambda}_i^2$ is the ith complex eigenvalue for this system and $\underline{Q} = \underline{\underline{\tilde{\psi}}}^{HT}\underline{F}$. The steady-state harmonic solution to each of the decoupled equations of motion in Eq. (14) is given as follows, where i =1, 2, 3… 11:

$$\eta_i = \frac{Q_i}{\lambda_i^2 - \omega^2}. \tag{15}$$

Table 3. Modal force vectors for in-phase and out-of-phase cases.

Mass element in Fig. 7	Vector for in-phase case	Vector for out-of-phase case
m_v	0	$2\phi_{dl}^{(1)}F_1$
m_θ	$2\phi_{dl}^{(2)}F_1$	0
m_{bl}	$2\phi_{dl}^{(3)}F_1$	0
m_{br}	0	$2\phi_{dl}^{(4)}F_1$
m_{gl}	$2\phi_{dl}^{(5)}F_1$	0
m_{gr}	0	$2\phi_{dl}^{(6)}F_1$
m_{sl}	$2\phi_{dl}^{(7)}F_1$	0
m_{sm}	0	$2\phi_{dl}^{(8)}F_1$
m_{sr}	$2\phi_{dl}^{(9)}F_1$	0
m_{dl}	$2\phi_{dl}^{(10)}F_1$	0
m_{dr}	0	$2\phi_{dl}^{(11)}F_1$

The steady-state physical response of the damped system is then calculated using a formula similar to Eq. (6). Like the undamped case, each term of the response is compared against the total physical domain response. The addition of damping reduces the amplitude of the resonant peaks as expected; only 6 modes participate for the in-phase case, and the remaining 5 modes participate for the out-of-phase case, as observed in the undamped case. The eigenvectors corresponding to the spindle masses are analyzed, and the corresponding force vectors Q_i are found to be similar to the minimally damped case. From Table 2 it can also be observed that due to the left-right symmetry in the system, the eigenvectors corresponding to m_{dl} and m_{dr} are always equal in magnitude and remain unaffected by the damping. The dynamic forces at the modes either add or cancel each other out to produce modal forces as reported in Table 3, explaining the participation of the modes and excitation phasing for different excitation cases. Additionally, the harmonic responses are studied for 3 additional phase angles between 0 and 180 degrees between the left and right spindles, given equal amplitudes of excitation. It is expected that changing the excitation phasing would directly influence the way the modes participate, similar to what was observed with the in-phase and out-of-phase cases.

Next, the acceleration hatch plots at the subframe left mass m_{bl} are displayed in Fig. 11 for two cases: (i) only the in-phase and out-of-phase responses and (ii) for 5 phasing cases (0, 45, 90, 135, 180 degrees). The in-phase and out-of-phase responses overlap with the hatch plots using all five phasing cases, with the exception of a few small frequency bands. This implies that the in-phase and the out-of-phase cases are sufficient to predict the upper and lower bounds of harmonic responses.

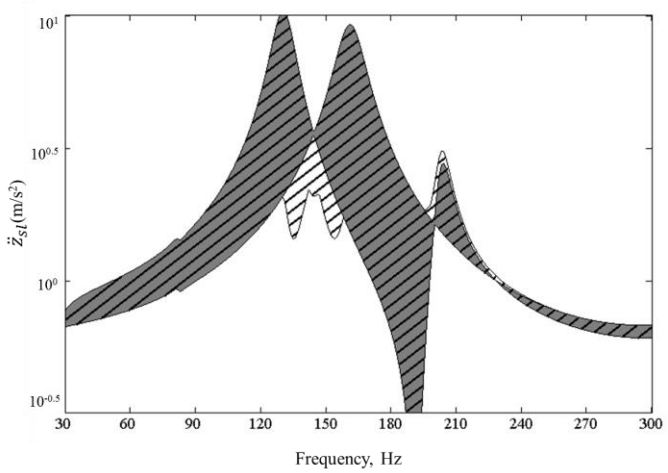

Figure 11: Comparison between in-phase and out-of-phase hatch plots against all phasing hatch plots for the lumped vehicle model: ▬, in-phase and out-of-phase; ▨ , all phasing cases.

Forced response from finite element model under harmonic excitation

Forced response studies are conducted using the reduced order finite element model. Five cases of excitation phase differences (0, 45, 90, 135 and 180 degrees) are considered for this finite element model. Upon comparing the hatch plots in Fig. 12, it is observed that the response from the in-phase and out-of-phase cases encompass all the other phasing cases. Fig. 13(a) displays the spectra for the vertical

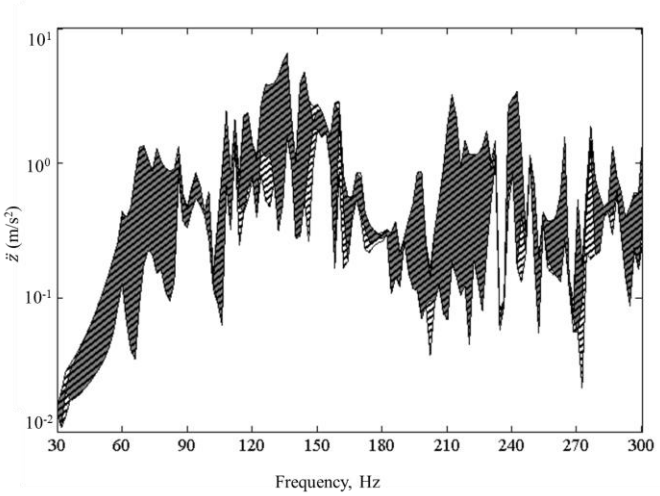

Figure 12: Comparison between in-phase and out-of-phase hatch plots against all phasing hatch plots for the acceleration spectra ($\ddot{z}$, m/s^2) at location 1 on the subframe from finite element analyses: ▬, in-phase and out-of-phase case; ▨, all phasing cases.

acceleration response at location 1 of the subframe for both in-phase and out-of-phase cases. Like Fig. 3(b), Fig. 13(b) is a hatch plot where the upper and lower limits are formed by computing the maximum and minimum responses from the in-phase and out-of-phase excitation cases (with a 1-Hz resolution). Note that the input phasing significantly affects the acceleration responses at the subframe with variations as large as 30 dB from 180 to 250 Hz, as shown in Fig. 13(c). These results correlate reasonably well with variations predicted by the lumped model, thus verifying the minimal order vehicle model.

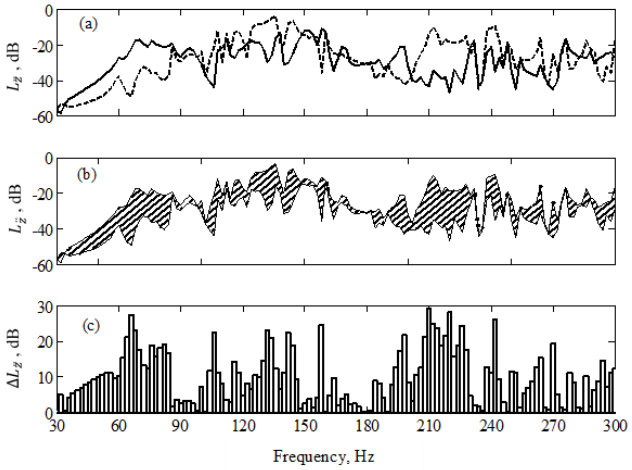

Figure 13: Computed acceleration spectra from finite element model ($L_{\ddot{z}}$, dB re 1.0 g rms) at location 1 on the subframe for different phasing cases shown at 2-Hz resolution: (a) phase variations: ——, 0°; ----,180°; (b) hatch plot representation of phasing variations; (c) difference between maximum and minimum acceleration response at each frequency.

Comparison of predicted and measured results

Since the tires and wheels are being ignored in this model, measured operational displacements at a roller speed of 80 kph are used as excitations and implemented as follows: 1. First, the dynamic excitations are described by harmonic vertical displacements z_1 and z_2 of unit amplitudes at the left and right spindle centers at any frequency of calculation; 2. A steady-state dynamic analysis (with the same damping assumptions as before) is over the frequency range of 30-300 Hz; 3. Assuming the linear system theory, the corresponding harmonic acceleration responses are calculated at the body connections and normalized by the excitation acceleration amplitudes ($-\omega^2 z_1$ or $-\omega^2 z_2$) at each frequency; 4. The normalized acceleration response is then scaled by the acceleration measured at the spindle center for one of the runs, $\ddot{z}_d$, from the chassis dynamometer experiment. This is needed to compare the computed responses with measurements.

The predicted acceleration responses from the finite element model are now compared with the measurements. The computed hatch plots from the in-phase and out-of-phase responses are compared with measurements in Fig. 14 at locations 1, 2 and 3 on the subframe. The

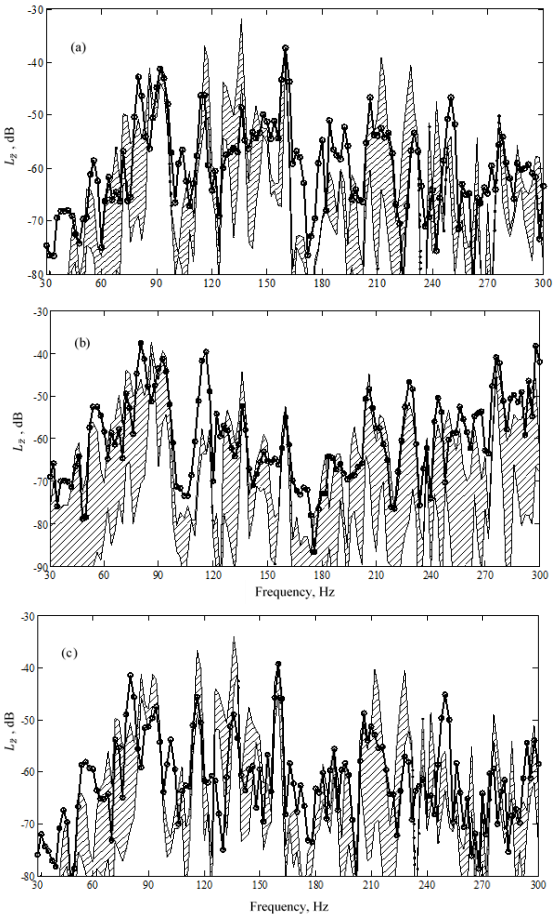

Figure 14: Comparison of measured and computed vertical acceleration spectra ($L_{\ddot{z}}$, dB re 1.0g rms) at different locations on the subframe (hatch plot using in-phase and out of phase cases): (a) location 1; (b) location 2; (c) location 3: **-o-**, Measured response; ▨, Computed response from the finite element model.

measured spectral points are observed to fall within the computed hatch plots with discrepancies at some narrow-frequency bands, suggesting that the calculation method yields a reasonable prediction. However, in Fig. 14(b), note that the simulation provides resonant peaks well, but the computations do not fall within the measured range at other frequencies. This could imply that damping values in the finite element model need to be refined, as this component has a dominant participation in this particular frequency range of study.

The finite element operational deflection shapes are examined to visualize the subframe dynamics corresponding to the response variations associated with excitation phasing. Based on average variations due to phasing at six different locations on the subframe, two particular frequencies (220 Hz and 236 Hz) are chosen – one where variations due to phasing are large and the second where variations are relatively small. Four views (top, front, left and right) are displayed for the deflection shapes, and a comparison is made between the in-phase and out-of-phase deflection shapes in Fig. 15. The subframe has small deflections for the in-phase case (Fig. 15(a)), whereas the subframe exhibits a large rocking motion when viewed from the top for the out-of-phase condition shown in Fig. 15(b). In contrast, the subframe has minimal variation in the deflection shapes for both in-phase and out-of-phase excitation at 236 Hz. Overall, the participation of the subframe is qualitatively similar to that observed experimentally, suggesting that the ODS displays are an efficient way to evaluate subframe dynamics.

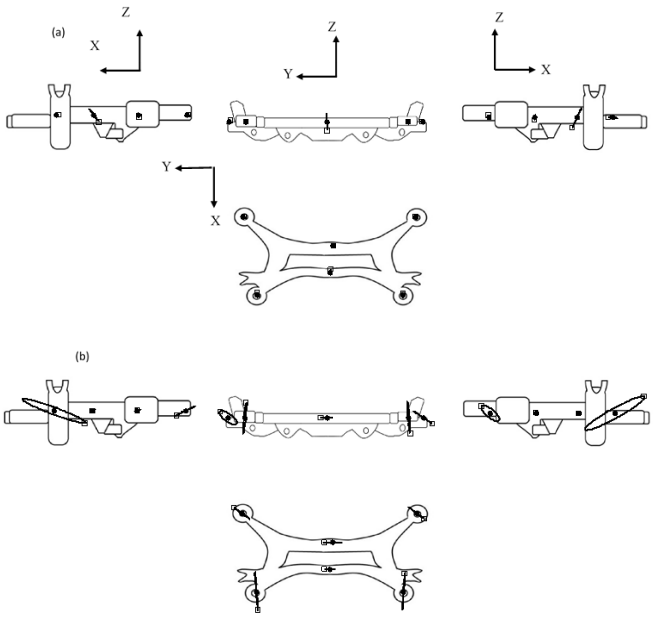

Figure 15: Calculated operational deflection shape of the subframe from finite element simulation at 220 Hz: (a) in-phase; (b) out-of-phase: ●, locations on the subframe where deflections are calculated; □, trajectory starting point (at t = 0); —, trajectory.

Conclusion

This article has contributed to the state-of-the-art by providing an in-depth investigation and explanation of the role of the left-right rolling excitation phasing at the spindles in the variability of automotive structure-borne vibration and noise (over the lower-frequency regime). Unlike prior literature, by limiting the operational experiments on a single vehicle, relationships between spindle excitations and run-run variations could be analyzed using a deterministic approach. A minimal order lumped parameter model of the rear-half vehicle, capturing the subframe transfer path, is successfully developed and is utilized to study the contribution of the subframe dynamics under dynamic loading conditions. Through the forced response analysis of this lumped parameter model using a deterministic modal expansion method, it is demonstrated that system vibration modes may cancel or add depending upon the left-right magnitude and phasing of excitations going into the system through the spindle (i.e., this is a deterministic phenomenon), which in turn has variations up to +/- 30 dB. In addition to this, both the lumped model and the finite element models are consistent in suggesting that two cases of phasing, namely in-phase and out-of-phase, are necessary and sufficient to predict a range for the system response. Operational deflection shapes have successfully been employed to qualitatively compare the variations due to phasing observed in the finite element results and the run-run variations observed in the steady-state vehicle measurements. This suggests that the run-run variations could be significantly influenced by the magnitude and phase of the tire-road interactions, which in turn control the magnitude and phase at which the excitations travel through the suspension system starting at the spindle. As part of future work, this deterministic left-right phasing phenomenon could be further validated by conducting operational experiments, with focus on controlling the excitation phasing. Currently, the post-processing and windowing techniques used during data acquisition to compute the frequency spectra use as high as 50 averages on data acquired over 25 seconds to account for the probabilistic nature of the excitations. The sensitivity of the run-run variations to the type of signal processing (including windowing techniques) needs to be examined in the future. In addition, measurements may be acquired over a longer period of time, with minimal or no averaging, to study the deterministic nature of the excitations.

References

1. Lalor, N. and Prieibsch, H.H., "The prediction of low and mid-frequency internal road vehicle noise: a literature survey," *Proc. IMechE Part D: J. Automobile Engineering.* 221(3): 245-269, 2007.
2. Kuijpers, A.H. and Van Blokland, G., "Tyre/road noise models in the last two decades: a critical evaluation," *Proc. INTER-NOISE.* 2001: 2593-2598, 2001.
3. Kompella, M.S. and Bernhard, R.J., "Measurement of the statistical variation of structural-acoustic characteristics of automotive vehicles," SAE Technical Paper 931272, 1993.
4. Gaardhagen, B. and Plunt, J., "Variation of vehicle NVH properties due to component eigenfrequency shifting-basic limits of predictability," SAE Technical Paper 951302, 1995.
5. Connelly, T., Knittel, J., and Jay, M., "A study of NVH vehicle testing variability," SAE Technical Paper 2005-01-2553, 2005.
6. Shaver, R.M., Liu, K.J., and Hardy, M.G., "Vehicle-to-vehicle NVH performance variance," SAE Technical Paper 2009-01-2179, 2009.
7. Wood, L.A. and Joachim, C.A., "Variability of interior noise levels in passenger cars," *IMechE conference on vehicle noise and vibration*: 197-206, 1984.
8. Hills, E., Mace, B. R., and Ferguson, N. S., "Acoustic response variability in automotive vehicles," *Journal of Sound and Vibration*, 2009; 321(1-2): 286-304.
9. Li, B., Yang, X., Yang, J., "Tire model application and parameter identification- a literature review," *SAE Int. J. Passenger Cars-Mechanical Systems*. 7(1):231-43, 2014.
10. Abaqus/CAE (Version 6.13), Computer Software, Dassault Systems Simulia, Providence, RI, 2013.

11. de Klerk, D. and Ossipov, A., "Operational transfer path analysis: theory, guidelines and tire noise application," *Mechanical Systems and Signal Processing* 2010; 24(7): 1950-1962.
12. Meirovitch, L., "Fundamentals of vibrations," (New York, McGraw-Hill, 2002).

Contact Information

Professor Rajendra Singh
Acoustics and Dynamics Laboratory,
NSF I/UCRC Smart Vehicle Concepts Center
Dept. of Mechanical and Aerospace Engineering
The Ohio State University

E-mail: singh.3@osu.edu
Phone: 614-292-9044
Website: www.AutoNVH.org

Acknowledgments

The authors gratefully acknowledge the National Science Foundation Industry/University Cooperative Research Centers program (www.nsf.gov/eng/iip/iucrc) for partially supporting this research via the Smart Vehicle Concepts Center (www.SmartVehicleCenter.org). Other organizations that provided support (and mentorship) include F.Tech R&D and Honda R&D.